https://doi.org/10.26599/JAC.2024.9220912

Research Article

Control of electromechanical performance in 3D printing lattice-structured $BaTiO_3$ piezoelectric ceramics

Zhujun Jiang [a, b, †], Yinghong Sun [a, b, †], Jimin Chen [a, b, *], Yong Zeng [a, b, *]

[a] Faculty of Materials and Manufacturing, Beijing University of Technology, Beijing 100124, China

[b] Beijing Engineering Research Center of 3D Printing for Digital Medical Health, Beijing 100124, China

[†] Zhujun Jiang, Yinghong Sun: These authors contributed equally to this work.

[*]Corresponding authors

E-mail: J. Chen, jimin@bjut.edu.cn

Y. Zeng, watnd@163.com

Received: February 08, 2024; Revised: May 10, 2024; Accepted: May 11, 2024

Abstract:

Barium titanate ($BaTiO_3$) piezoelectric ceramics with triply periodic minimal surfaces (TPMS) structure have been frequently used in filters, engines, artificial bones, and other fields due to their high specific surface area, high thermal stability, and good heat dissipation. However, only a limited amount of studies have analyzed the effect of various parameters such as different wall thicknesses and porosities of TPMS structures on the ceramic electromechanical performance. In this study, we first employed Vat photopolymerization (VPP) 3D printing technology to fabricate high-performance $BaTiO_3$ ceramics. We investigated the slurry composition design and forming process, and designed a stepwise sintering post-processing technique to achieve a density of 96.3% and a compressive strength of 250 ± 25 MPa, with the piezoelectric coefficient (d_{33}) reaching 263 pC/N. Subsequently, we explored the influence of three TPMS structures, namely Diamond, Gyroid, and Schwarz P, on the piezoelectric and mechanical properties of the $BaTiO_3$ ceramics, with the Gyroid structure identified as exhibiting optimal performance. Finally, we examined the piezoelectric and mechanical properties of Gyroid structure $BaTiO_3$ ceramics with varying wall thicknesses and porosities, thus enabling the modulation of ceramic electromechanical performance.

Keywords

3D printing, piezoelectric ceramics, porous structure, mechanical properties, electrical properties

1. Introduction

$BaTiO_3$ ceramics have been widely employed as representative lead-free piezoelectric ceramics due to their high dielectric constants, low dielectric losses, and high mechanical conversion performance [1]. $BaTiO_3$ ceramics are used in various fields such as sensors [2], renewable energy [3], and multilayer ceramic capacitors [4], serving as one of the most extensively utilized electronic ceramic materials and earning the epithet "the backbone of the electronic ceramic industry". Since Roberts et al. first reported on the piezoelectric behavior of polarized $BaTiO_3$ ceramics, research in this field has rapidly progressed rapidly. Scholars have explored specific application requirements by improving the preparation methods [5], ion element doping [6], introducing secondary phases [7], incorporating porosity [8], and designing different structures [9]. However, with industrial advancements demanding miniaturization and lightweight microelectronics technology, there is increasing demand for high-performance barium titanate ceramics characterized by large surface areas, light weight, and superior mechanical properties. Traditional piezoelectric ceramic forming methods mainly include dry pressing, hot pressing, isostatic pressing, casting, and casting. After forming, the ceramic body must be densified by heat treatment and subjected to mechanical processing. However, due to the high brittleness and high melting point of ceramics, it is difficult for traditional molding methods to prepare complex three-dimensional structures, making it difficult to meet the comprehensive requirements of miniaturization, as well as controllable precision and structure.

Three-dimensional (3D) printing is a digital manufacturing technology that directly shapes 3D complex structures by adding materials layer-by-layer in two dimensions. This technology can control the three-dimensional macroscopic structure and porosity of piezoelectric materials, and obtain complex special-shaped (i.e., curved surface, inner hole) ceramic material structures without the need for molds. In recent years, techniques such as Fused Deposition Modeling (FDM), Direct Inkjet Writing (DIW), and Stereolithography Apparatus (SLA) have been used for ceramic part manufacturing. Dejana et al. [10] combined a candidate material comprised of thermoplastic polyurethane (TPU) and carbon black (CB) with piezoelectric elements such as polyvinylidene fluoride (PVDF) and $BaTiO_3$, which possessed conductivity and flexibility, and evaluated their suitability in sensor applications without the need for polarization. Chen et al. [11] utilized DIW technology to prepare multi-level porous structure polydimethylsiloxane (PDMS)/ $BaTiO_3$ composite materials with ultra-high $BaTiO_3$ content and superior toughness. Sotov et al. [12] developed a ceramic slurry preparation technique suitable for LCD-SLA printing and tested three types of $BaTiO_3$ powders (micron-sized, submicron-sized, and nano-sized) utilizing LCD-SLA 3D printing technology. However, each of these techniques has drawbacks. For example, FDM technology suffers from the low solid loading of piezoelectric ceramic slurries, while DIW exhibits low printing accuracy, and SLA technology faces limitations related to the viscosity and photosensitivity of liquid resins.

Vat photopolymerization (VPP) 3D printing technology has emerged in recent years as a promising ceramic 3D printing technique capable of producing high-precision and complex ceramic specimens [13–16]. Compared to other traditional 3D printing technologies, VPP 3D printing technology exhibits higher efficiency, higher print quality, reduced material waste, and greater design freedom. Studies have demonstrated the VPP preparation effectiveness of ceramic materials and the feasibility of high-quality ceramic body sintering [17–22]. He et al. [23] leveraged VPP technology to successfully manufacture a complex triangular zirconia tool with reset grooves and honeycomb ceramic parts, exhibiting a Vickers hardness of 13.0597 GPa. Chen et al. [24] also utilized this technology to fabricate high-performance broadband microwave-transparent Si_3N_4-SiO_2 composite ceramics. Additionally, Yao et al. [25] successfully employed 3D printing technology to prepare hydroxyapatite (HA) ceramics with excellent densification and mechanical properties, thus, laying a solid foundation for bone engineering applications.

VPP technology has also been used for the fabrication of co-continuous structured piezoelectric composite ceramics. Liu et al. [26] investigated the performance of photosensitive slurries from the perspective of particle size distribution to enhance the density and piezoelectric constant of $BaTiO_3$ ceramics prepared using 3D printing, leading to the fabrication of TPMS structured $BaTiO_3$ ceramics. We previously utilized VPP technology to fabricate $BaTiO_3$ traditional truss structures with porosities ranging from 10% to 90%, and preliminarily studied the influence of different porosities on their electromechanical properties [27]. However, limited research has been conducted on the

optimization of TPMS structures and the analysis of parameters such as different wall thicknesses and porosities, to control the electromechanical properties of ceramics.

This study systematically investigated the formulation design of $BaTiO_3$ photocurable ceramic slurries and the molding process. Additionally, we analyzed and optimized the degreasing and sintering parameters of $BaTiO_3$ green bodies to determine the feasibility of photocurable preparation for piezoelectric $BaTiO_3$ ceramics. The finite element method was applied to numerically simulate the stress and generated electrical signals of porous ceramics. The study then examined the strain mechanisms of configuration units and porosity under stress in various microstructures, to explore their electromechanical coupling effects on $BaTiO_3$ porous structure piezoelectric ceramics. Furthermore, piezoelectric ceramics with different wall thicknesses and porosities in the TPMS structures were printed, and their mechanical and electrical properties were tested. Comparative analysis with the simulation results allowed for the regulation of ceramic electromechanical performance, facilitating their application in devices for diverse requirements and applications. This study provides a foundation for the practical application of complex-structured barium titanate ceramics fabricated via photocuring.

2. Materials and methods

2.1. Materials

The $BaTiO_3$ slurry consisted of $BaTiO_3$ powder ($\geq$ 99.9% purity) with a powder particle size of 200 nm (Shanghai Macklin Biochemical Co., Ltd., China), acrylic resin (Trimethylolpropane Triacrylate, TMPTA, Shanghai Aladdin Bio-Chem Technology Co.,

Ltd., China), photoinitiator (Ethyl 4-dimethylaminobenzoate, Shanghai Aladdin Bio-Chem Technology Co., Ltd., China), and dispersant (BYK-111, produced by BYK Additives (Shanghai) Co., Ltd China). The composition of the slurry and its proportions are shown in Table 1.

Table 1. Composition of the $BaTiO_3$ slurry.

Materials	State	Function	Content (vol.%)
$BaTiO_3$	Powder	Ceramic matrix	45.00
TMPTA	Liquid	Acrylic resin	52.38–52.47
Ethyl 4-dimethylaminobenzoate	Powder	Photoinitiator	0.03–0.12
BYK-111	Liquid	Dispersant	2.50

2.2. Preparation of the $BaTiO_3$ slurry

The $BaTiO_3$ raw powder was dried in a drying oven at 80 °C for 3 h. The dried powder material and dispersant were then placed in a ball milling tank and mixed by ball milling for 3 h with anhydrous ethanol as the medium. The ball milled mixture was then dried in a drying oven at 60 °C for 24 h to obtain the dried modified barium titanate powder. The modified powder was mixed with photosensitive resin and photoinitiator, and subsequently fully mixed with homogenizer to obtain ceramic slurry with uniform components. The above mixture was then ball-milled in a ball milling tank at 1500 r/min for 90 s to obtain the ceramic slurry.

2.3 Printing and post-processing

In this experiment, we utilized a top-down VPP 3D printer with a wavelength of 450 nm (CeraFab 7500, LITHOZ, Austria). This process involved placing the pre-configured ceramic slurry in the slurry tray, exposing it to the light source to initiate cross-linking in the photosensitive resin, forming a solid layer and completing one layer of the printed pattern. The build platform then moved upward by the thickness of one printing layer, and the scraper rotated two turns, ensuring that there was sufficient ceramic slurry below the build platform for the next curing cycle. This process was sequentially repeated to completely print the entire part.

After printing, excess slurry that adhered to the surface of the green body was removed using compressed air. Figure 1a depicts the Thermo Gravimetric (TG) and Differential Thermo-Gravimetric (DTG) curve of the printed green body. The TG-DTG curve was carried out in an argon atmosphere with a flow rate of 10 mL/min and a heating rate of 10 °C/min. The test temperature range was from room temperature to 800 °C. The degreasing curve was optimized and designed according to the analysis of the TG-DTG curve, as illustrated in Figure 1b. The temperature increase rate was set to 1 °C/min under an argon atmosphere, and the temperature was held at 205 °C, 445 °C, and 800 °C for 60 min, 60 min, and 30 min, respectively. In this experiment, different sintering processes were implemented to enhance their densities, and ordinary sintering and two-step sintering methods were used for the sintering process. This resulted in the preparation of different $BaTiO_3$ piezoelectric ceramic parts [28]. Figure 1c shows the ordinary sintering curve. Before reaching 800 °C, the heating rate was 2 °C/min. At 800 °C, the heating rate

was adjusted to 1.5 °C/min to reach temperature T_1, with a holding time (t_1) of 3 h. Figure 1d illustrates the two-step sintering curve, where the rate of temperature increase from room temperature to T_1 matched that of ordinary sintering. However, unlike ordinary sintering, no holding occurred at temperature T_1. Instead, the temperature was reduced at a rate of 5 °C/min to temperature T_2, where it was held for 15 h (t_2), before cooling in the furnace.

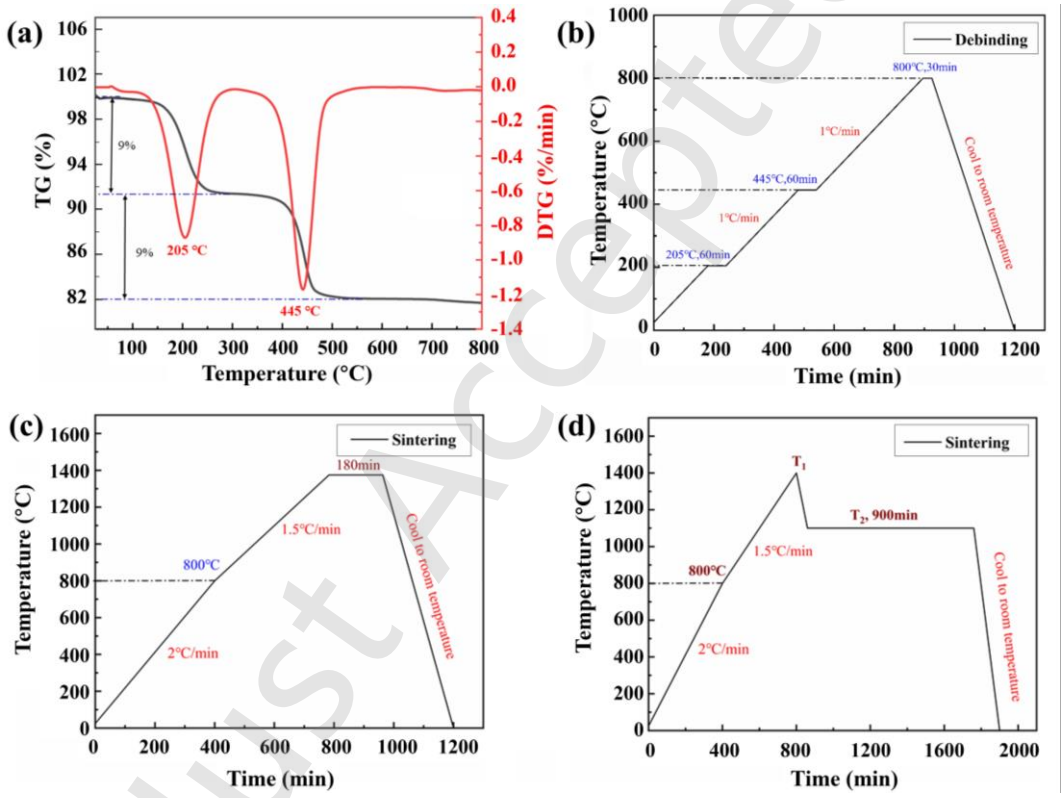

Figure 1. $BaTiO_3$ heat treatment process: (a) TG-DTG curves of the $BaTiO_3$ ceramic billets; (b) degreasing curves of the billets; sintering curves of $BaTiO_3$: (c) normal sintering; (d) two-step sintering.

For phase analysis of the sintered samples, additional steps such as surface polishing and gold coating were possibly required. Special property tests, such as piezoelectric, ferroelectric, and dielectric properties, possibly necessitated further surface treatments

such as silver paste application and high-voltage polarization. The specific steps for polarization were as follows. The samples with silver paste-coated surfaces were placed into a high-voltage polarization device (ET2673D-4, Nanjing Entai Electronic Instrument Factory, China). Polarization was subsequently carried out under a high-voltage electric field (1.5 kV/mm) for 30 min.

2.4 Characterization

At room temperature, the rheological viscosity of the slurry was measured using a rotational viscometer (NDJ-5S, Min Test Instrument Equipment (Xiamen) Co., Ltd., China). This test characterized the rheological properties of the slurry for different types and varying concentrations of dispersants, as well as different solid contents. Comprehensive thermal analysis of the samples was then conducted using a simultaneous thermal analyzer (STA-449C, NETZSCH, Germany), which included TG-DTG tests. The crystal structures of the ceramics were analyzed by X-ray diffraction (XRD) using an X-ray diffractometer (D8 Advance, Bruker, Germany). The density of the sintered ceramic was measured by the drainage method, according to the Archimedes principle. Surface and cross-sectional morphology analysis of the ceramic samples was performed using a scanning electron microscope (SEM) (SU8020, Hitachi Corporation, Japan). The piezoelectric coefficient of the ceramic components was measured at room temperature using a quasi-static piezoelectric coefficient d_{33} tester (ZJ-4A, Institute of Acoustics, Chinese Academy of Sciences). The dielectric properties were also tested and analyzed using a precision impedance analyzer (LCR, 4294A, Agilent, USA), and the ferroelectric

properties of the post-sintered samples were characterized using a ferroelectric analyzer (aixACCT TF2000, Radiant Technologies, USA). The compressive and flexural strengths of the samples were determined by a universal material testing machine (Zwick/Roell Z100, Zwick-Roell, Germany).

3. Results and discussion

3.1. Analysis of the morphology and light-curing properties of the $BaTiO_3$ ceramic pastes

In this study, BYK-111 was selected as the dispersant, and the impact of BYK-111 dosage on the dispersion effect in the slurry was investigated and optimized. Figure 2a shows the relationship between the viscosity and dispersant content at a shear rate of 30 s^{-1}. The experiments revealed that with less than 3 vol% dispersant content, the viscosity of the slurry decreased as the dispersant content increased. However, when the dispersant content exceeded 3 vol%, the viscosity of the slurry increased with the dispersant content. Despite the lowest dispersant content of 3 vol% with a viscosity of 899 mPa·s, lower viscosity did not necessarily fall within the suitable viscosity range for light-cured ceramic printing. Rather, the photosensitive resin plays a curing role, especially during the exposure curing printing process. Excessive dispersant in the ceramic system possibly had some impact on the final formation quality and precision. At a dispersant content of 2.5 vol% in the slurry, the system exhibited an optimal viscosity value of 2482 mPa·s, which fell within the viscosity range suitable for light-cured ceramic printing.

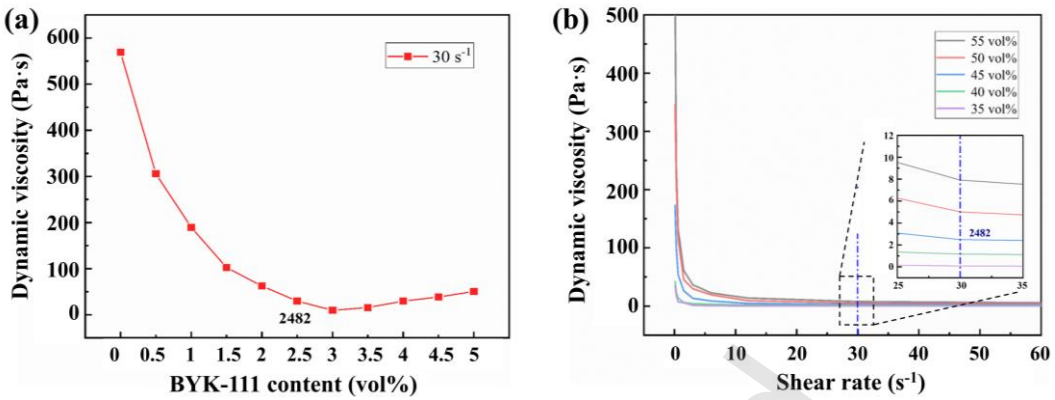

Figure 2. Viscosity of the $BaTiO_3$ slurry as a function of (a) BYK-111 content (shear rate of 30 s^{-1}) and (b) solid content.

The solid content also significantly affected the rheological properties of the ceramic slurry system. To achieve precise control over ceramic dimensions and minimize discrepancy between the formed dimensions and the theoretical model, it was important to formulate ceramic slurries with high solid content while meeting the viscosity requirements for light-cured shaping. In this experiment, BYK-111 at a concentration of 2.5 vol% was chosen as the dispersant, and the viscosity performance of the slurry at different solid contents was studied. Figure 2b shows the viscosity changes of the slurry at different solid contents. When the solid content exceeded 45 vol%, the viscosity significantly increased. This was because as the solid content increased, the proportion of resin that could flow within the slurry system decreased, resulting in a reduced liquid phase content surrounding the ceramic particles. This, in turn, increased the frictional resistance between the particles in motion within the system, leading to an increase in slurry viscosity. When the solid content reached 50 vol%, the viscosity exceeded the critical range suitable for VPP 3D printing, with a viscosity value of 5286 mPa·s at a shear

rate of 30 s^{-1}. Therefore, in this experiment, a solid content of 45 vol% was chosen as the optimal ceramic slurry composition.

Considering the effect of exposure energy on the depth of light curing, we assessed the relationship between the light time and the thickness of the light-cured layer and studied the curing depth of the light-cured forming ceramic slurry according to the Beer-Lambert law [29]. As shown in formula (1), we studied the relationship between exposure time and curing depth C_d by fixing the exposure light intensity W to 90mW/cm^2 and changing the exposure time t. The curing depth for different exposure times is measured using a digital caliper, with each exposure time being measured three times to obtain an average value. The resulting variation curve is shown in Figure 3a.

$$E_i = W \times t \tag{1}$$

E_i is the exposure energy of incident light (mJ/cm^2); W is the exposure light intensity (mW/cm^2); t is the exposure time (s).

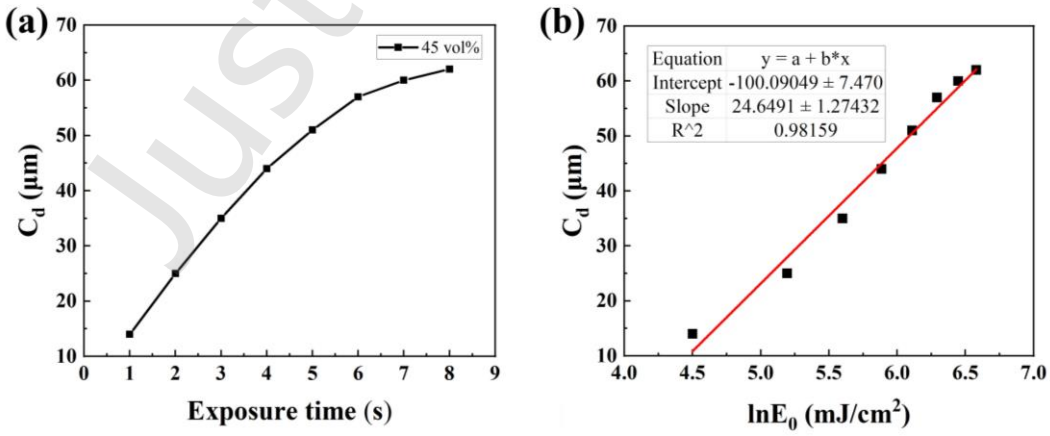

Figure 3. (a) Plot of cured layer thickness versus exposure time, (b) Beer-Lambert linear fitting results

The results were fitted and analyzed according to equation (2) using Beer-Lambert law. where lnE_0 was used as the horizontal coordinate and the thickness of the single cured layer as the vertical coordinate.

$$C_d = \mathrm{S_d} \ln\left(\frac{E_0}{\mathrm{E_d}}\right) \quad (2)$$

Where C_d is the thickness of a single cured layer; E_d is the critical exposure energy; E_0 indicates the actual exposure energy of the slurry cure, which is equal to the product of the exposure light intensity and the exposure time; and S_d is the photosensitivity parameter, which reflects the sensitivity of the ceramic slurry to light.

Figure 3b illustrates the Beer-Lambert linear fitting results for ceramic pastes. There is a positive proportionality between the thickness of the cured layer and the logarithm of the exposure energy. According to the fitting results, the slope S_d is 24.65 and the intercept -$S_d$lnE_d is -100.09, so the curing equation of $BaTiO_3$ ceramic paste in this experiment is obtained as shown in equation (3):

$$C_d = 24.65(lnE_0 - ln58) \quad (3)$$

According to this equation, the critical exposure energy value in this experiment is 58 mJ/cm^2. This value can provide guidance for the subsequent printing work based on the desired layer thickness. However, it's important to note that in the actual printing process, to ensure adhesion between layers, the actual layer thickness printed is generally around half of the single-layer curable thickness. In this study, the thickness of the slice layer was 25 μm and the exposure energy was 500 mJ/cm^2 for printing. Additional details are provided in the supporting materials.

3.2 Analysis of the physical phase, micro-morphology, mechanical and electrical properties of ceramics with different post-processing regimes

Table 2 shows the shrinkage of the $BaTiO_3$ ceramic samples prepared under different sintering regimes in the X, Y, and Z directions. Measurements of size changes before and after sintering were obtained using calipers for each sintering regime. Each group of samples was tested using five specimens, and the average values were used to determine the shrinkage rates. We observed that the ceramic samples exhibited different shrinkage rates along the X, Y, and Z axes after sintering. For conventional sintering, the maximum shrinkage occurred at 1375 °C, with shrinkage rates of 18.2% along the X and Y directions and 28.3% along the Z direction. In the two-step sintering process, maximum shrinkage occurred in sample 9 at T_1 = 1400 °C and T_2 = 1200 °C, with shrinkage rates of 19.2% along the X and Y directions, and 28.5% along the Z direction.

Table 2. Different sintering methods for the preparation of $BaTiO_3$

Sample number	T_1(°C)	t_1(h)	T_2(°C)	t_2(h)	Sample Abbreviations	X-direction shrinkage (%)	Y-direction shrinkage (%)	Z-direction shrinkage (%)
Sample 1	1325	3	0	0	1325 °C-3h	17.2	17.2	27.6
Sample 2	1350	3	0	0	1350 °C-3h	17.5	17.5	28.1
Sample 3	1375	3	0	0	1375 °C-3h	18.2	18.2	28.3
Sample 4	1400	3	0	0	1400 °C-3h	18.0	18.0	27.9
Sample 5	1350	0	1100	15	1350-1100	17.4	17.4	28.2
Sample 6	1350	0	1200	15	1350-1200	17.6	17.6	28.4

Sample 7	1350	0	1300	15	1350-1300	19.1	19.1	28.4
Sample 8	1400	0	1100	15	1400-1100	19.0	19.0	28.5
Sample 9	1400	0	1200	15	1400-1200	19.2	19.2	28.5
Sample 10	1400	0	1300	15	1400-1300	19.1	19.1	28.5
Sample 11	1450	0	1100	15	1450-1100	19.0	19.0	28.4
Sample 12	1450	0	1200	15	1450-1200	18.9	18.9	28.4
Sample 13	1450	0	1300	15	1450-1300	18.9	18.9	28.4

Figure 4 illustrates the relative density and error charts for the two different sintering regimes. The density of the ceramic samples under different sintering regimes was measured using the Archimedes' principle, and the relative density was calculated, where the theoretical density of $BaTiO_3$ was 6.017 g/cm^3. Conventional sintering exhibited a dependency on the maximum sintering temperature. At lower sintering temperatures, the presence of more internal pores resulted in lower relative density. When the sintering temperature reached 1375 °C, the lowest porosity was achieved, resulting in the highest relative density of 93.9%. However, as the temperature increased further, the overall uniformity of the ceramic grains decreased, and some grains grew abnormally, with the possible presence of pores and secondary crystallization within the matrix, leading to a decrease in the relative density. In the two-step sintering regime, we observed that the holding time was more conducive to increasing the relative density of the ceramic. In previous reports, Wang et al. suggested that in the two-step sintering process, the first stage sintering temperature had a certain influence on grain size, while the second stage

sintering process, especially the holding time, was more favorable for increasing ceramic density [30]. Because the best sintering temperature of ordinary sintering was 1375 °C and the T_1 temperature of two-step sintering was less than 1375 °C, the grains did not obtain sufficient energy, even if the temperature was held for a long time, therefore, the density did not change significantly. When the T_1 temperature was greater than 1375 °C, the energy obtained by the system could realize the growth of the grains, thus, higher density could be obtained. However, when the temperature of T_1 was too high, the density slightly decreased, possibly due to the production of a portion of the liquid phase at higher temperatures, and secondary crystallization occurred. According to the density, we concluded that when the T_1 temperature was 1400 °C and the T_2 temperature was 1200 °C, the density was the highest at 15 h, with a value of 96.3%.

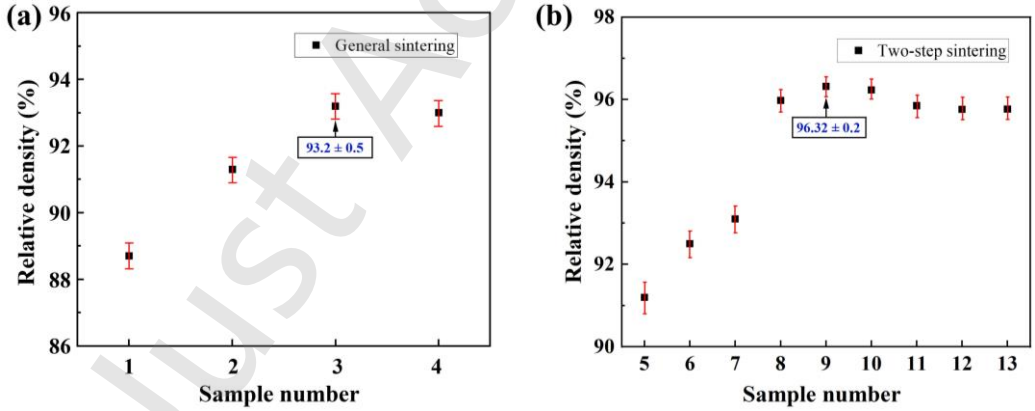

Figure 4. Densities of the samples prepared by different sintering methods: (a) normal sintering; (b) two-step sintering.

Figure 5a shows the XRD pattern of the ceramic samples prepared by conventional sintering. After comparing with the standard barium titanate card (PDF: 75–1606), we concluded that the samples consisted of pure $BaTiO_3$ without any impurities or phases

present. The intensity of diffraction peaks initially increased and then decreased with increasing sintering temperature, reaching its maximum at 1375 °C. This suggested that barium titanate could be successfully sintered at these temperatures, resulting in well-crystallized ceramics. By comparing the diffraction peak at $2\theta = 45°$, we observed that except for the case at a lower temperature of 1325 °C where the peak at 45° was not as distinct, the diffraction peak at 45° split into two peaks (002) and (200) at all other temperatures, indicating a typical tetragonal crystal structure. Upon closer observation, we noted a leftward shift in the peak positions, indicating an increase in lattice spacing and a gradual increase in the lattice parameters. This was possibly due to the increase in point defect concentrations inside the ceramic sample as the sintering temperature increased. The presence of defects caused a slight change in the lattice constant, especially the internal oxygen vacancies, which had an important effect. With an increase in sintering temperature, some oxygen vacancies were present in the interior, resulting in Ti^{+3} (0.72 Å) replacing Ti^{+4} (0.68 Å) of $BaTiO_3$ samples. This caused an increase in the lattice constant and lattice volume.

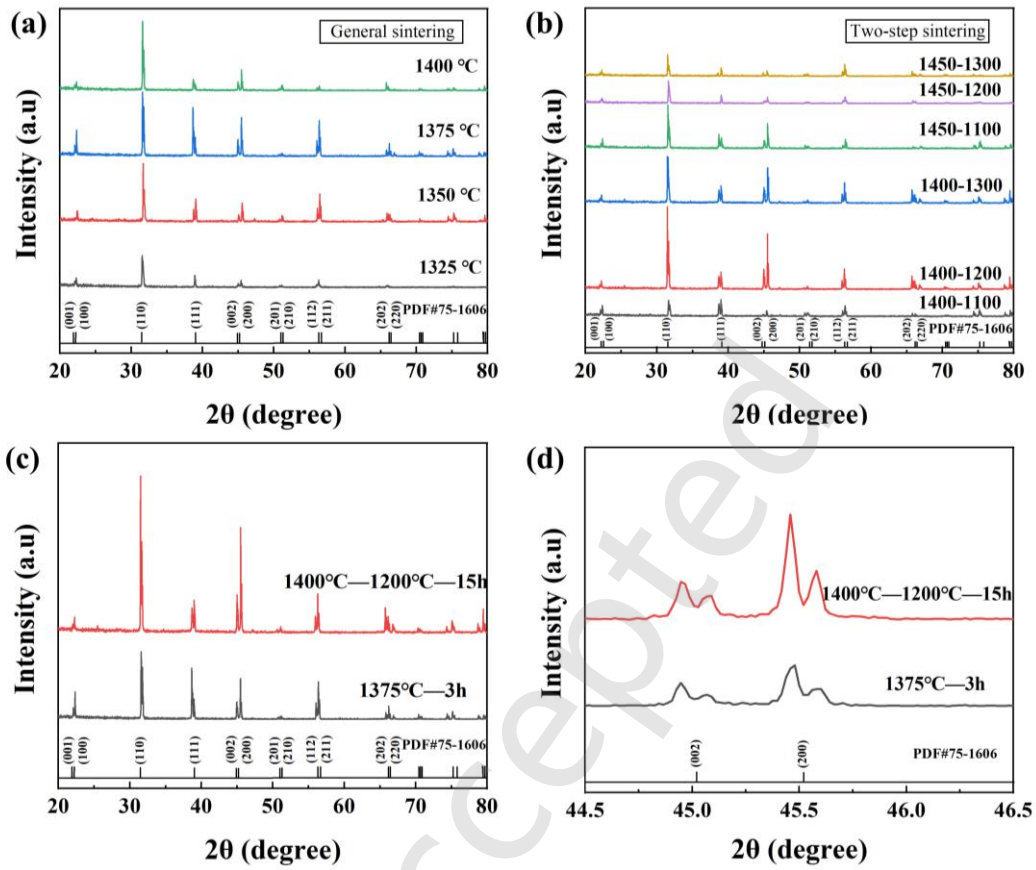

Figure 5. XRD diffractograms of the $BaTiO_3$ ceramic samples: (a) normal sintering; (b) two-step sintering; (c) comparison of the optimal sintering regimes for the two sintering regimes; (d) diffraction peaks at 2θ = 45°.

The XRD diffraction patterns of the $BaTiO_3$ ceramic samples prepared using the two-step sintering process are shown in Figure 5b. The results indicated a clear perovskite crystal structure, and the highest diffraction intensity was observed in the red line when the sample used a two-step sintering process at T_1 = 1400 °C and T_2 = 1200 °C. Figure 5c shows a comparison of the XRD patterns of the two different sintering methods for the optimal sintering conditions of both methods, indicating that the ceramic samples produced by the two-step sintering process had stronger diffraction peaks and better

crystallinity. Furthermore, as demonstrated in Figure 5d, the XRD peaks of the ceramic samples prepared by the two-step sintering process were sharper with narrower half-widths, indicating improved crystallinity under the specific sintering schedule. Among the five crystal phases of $BaTiO_3$, the tetragonal phase exhibited the best piezoelectric properties. According to these results, the optimal sintering method for preparing the $BaTiO_3$ piezoelectric ceramics was as follows. Initially, the temperature increased to 1400 °C, then rapidly cooled down to 1200 °C and maintained a long dwell time of 15 h.

Figure 6a–d shows the SEM images of the ceramics prepared by conventional sintering. As shown in the images, the surfaces of the ceramic samples sintered at different temperatures were relatively smooth. The smallest grain size was observed at 1325 °C, primarily due to incomplete sintering. As the sintering temperature gradually increased, the sintering process became more complete, leading to an increase in grain size. This was because the higher sintering temperature provided more energy for grain boundary migration and grain growth. However, beyond 1375 °C, a gradual formation of uneven grain sizes was observed. This was mainly attributed to excessively high sintering temperatures, which resulted in rapid grain boundary migration, causing some of the grains to grow rapidly and abnormally. This led to a reduction in surface density, ultimately impacting the performance of the material, and this result was consistent with the previous density analysis.

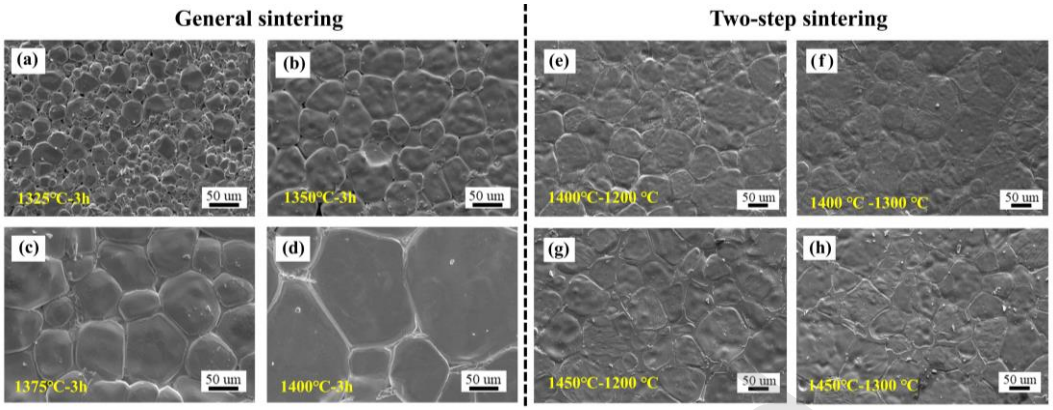

Figure 6. SEM images of the $BaTiO_3$ ceramics prepared by normal sintering: (a) 1325 °C-3h; (b) 1350 °C-3h; (c) 1375 °C-3h; (d) 1400 °C-3h; SEM images of the $BaTiO_3$ ceramics prepared by two-step sintering: (e) T_1 = 1400 °C, T_2 = 1200 °C (f) T_1 = 1400 °C, T_2 = 1300 °C; (g) T_1 = 1450 °C, T_2 = 1200 °C; (h) T_1 = 1450 °C, T_2 = 1300 °C.

Figure 6e–h shows the SEM images of the ceramics prepared by the two-step sintering process. We observed that their surfaces were relatively smooth, indicating good surface sintering quality. The grain sizes were relatively uniform and compared to the ceramics prepared by the conventional sintering process, bonding between the grains was superior. Figure 6e–f shows the ceramics prepared at a T_1 of 1400 °C and a T_2 of 1200 °C and 1300 °C, indicating that the grain size did not vary significantly between these conditions, however, at a T_2 of 1200 °C, more favorable grain uniformity and stronger bonding occurred between the grains. This was mainly because in the two-step sintering process, the grain size was primarily influenced by T_1, while T_2 and t_2 primarily affected the density of the material. Figure 6g–h depicts the ceramics prepared at a T_1 of 1450 °C and a T_2 of 1200 °C and 1300 °C. These two sets of data showed a slight increase in grain

size, however, their surfaces still exhibited a high degree of smoothness and uniformity, with good bonding between the grains, which was consistent with the density results.

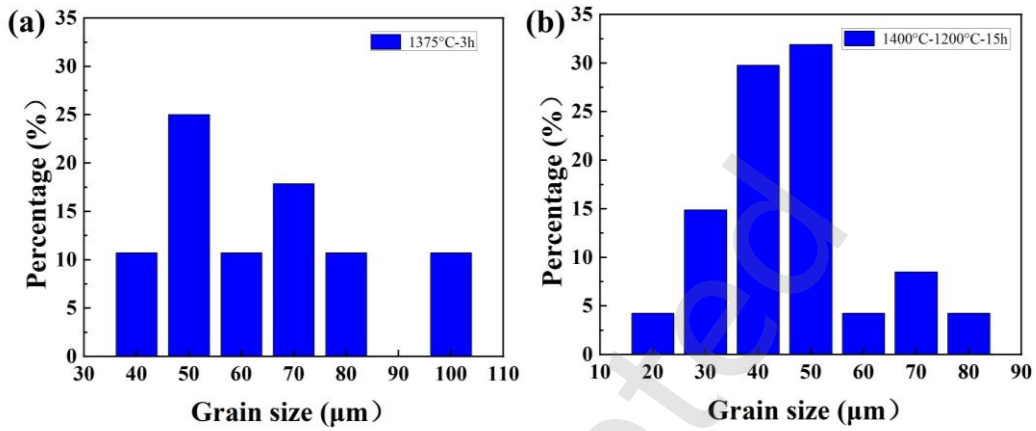

Figure 7. Grain size distribution of the sintered ceramics bodies: (a) 1375 °C-3h; (b)1400 °C-1200 °C-15h.

By analyzing the phase and microstructure of the piezoelectric ceramics, it was determined that the optimal sintering parameters for conventional sintering are sintering at 1375 °C for 3 h. For the two-step sintering process, the best parameters are ramping up to 1400 °C, followed by rapid cooling to 1200 °C and holding for 15 h. Figure 7 shows the grain size distribution of the ceramic under the optimal sintering parameters for ordinary sintering and the optimal sintering parameters for two-step sintering. We observed that the grains of two-step sintering were smaller and more evenly distributed, which further proved that the size and distribution of grains could be more accurately controlled by two-step sintering.

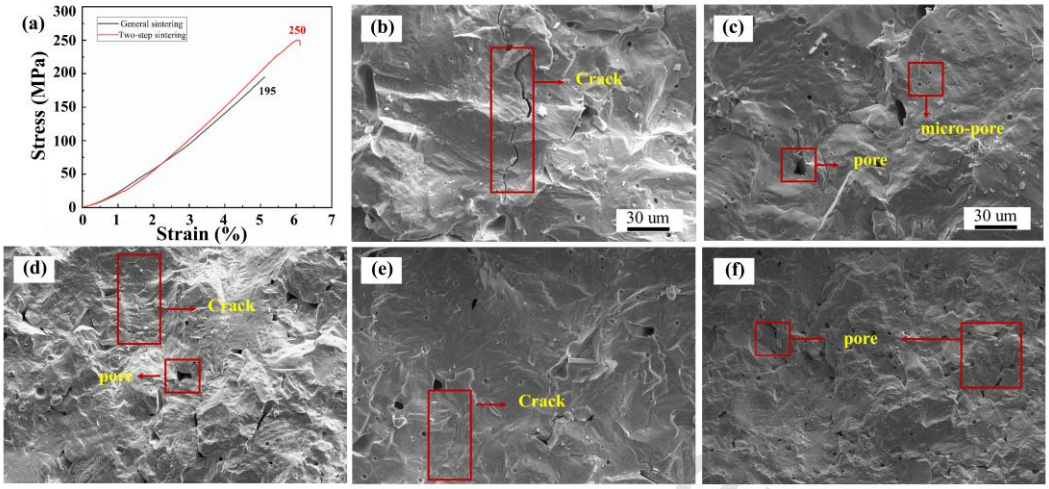

Figure 8. (a) Stress-strain diagrams of the solid blocks of $BaTiO_3$ ceramics; (b)–(f) SEM images of the fractured surfaces of the $BaTiO_3$ ceramics (T_1 = 1400 °C, T_2 = 1200 °C).

The maximum load-bearing capacity under operating conditions was considered for practical applications. Therefore, the mechanical properties of both sintering methods were compared, and compressive strength tests were performed. During the experiments, cylindrical $BaTiO_3$ ceramic specimens prepared by 3D printing were subjected to axial compression testing, and the obtained stress-strain curves are shown in Figure 8a. The compressive strengths were 250 ± 11 MPa for two-step sintering and 195 ± 8 MPa for conventional sintering. Figures 8b–f show SEM images of the brittle fracture surfaces, revealing the presence of the cracks, micro-pores, and voids as defects. The presence of pores at the grain boundaries could cause stress concentrations, leading to crack initiation. Therefore, when a ceramic material contained more internal pores, the more likely it was to form cracks under external forces. This also explained why samples with a higher density had higher compressive strength compared to ceramics with lower density.

To test the three-point flexural strength of the $BaTiO_3$ ceramic, a three-point flexural test was carried out on the samples prepared using the 3D printing process. The sample size was 36 mm (length) × 3 mm (width) × 4 mm (height). The decreasing speed of the indenter was 0.2 mm/min, and the force was applied in the printing direction with a span of 30 mm. The results showed that under the conventional sintering and two-step sintering processes, the samples had bending strengths of 24 ± 5 and 45 ± 8 MPa, respectively. In conclusion, the optimal sintering process for nanostructured barium titanate involved heating to a high temperature (T_1 = 1400 °C) and then cooling immediately for a long treatment time (15 h) at a low temperature (T_2 = 1200 °C).

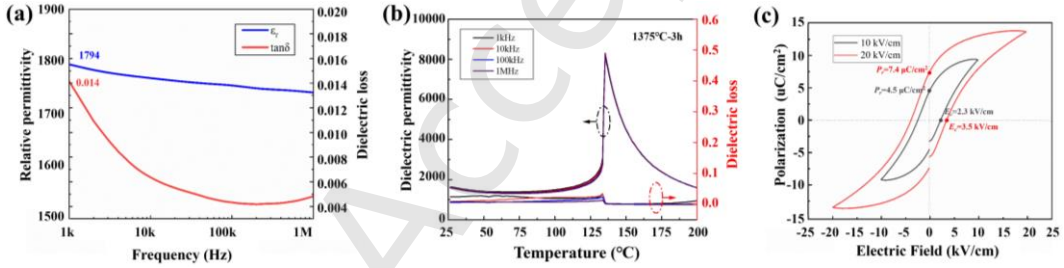

Figure 9. (a) Spectrum of the dielectric constant and dielectric loss of the $BaTiO_3$ ceramics at room temperature; (b) plot of the relative dielectric constant (ε_r) and loss ($tan\delta$) of the $BaTiO_3$ ceramics vs. temperature and frequency; (c) hysteresis echelons (P–E) of the $BaTiO_3$ samples at room temperature.

The relative permittivity (ε_r) and dielectric loss ($tan\delta$) frequency spectrum of the prepared barium titanate ceramic at room temperature are shown in Figure 9a. The sample size was 8 mm (length) × 8 mm (width) × 1 mm (height). The barium titanate ceramic exhibited a high relative permittivity and low dielectric loss, and a frequency of 1 kHz and room temperature, its relative permittivity and dielectric loss were 1794 and 0.014,

respectively. According to the graph, we observed that as the frequency increased, both the relative permittivity and dielectric loss of the $BaTiO_3$ ceramic gradually decreased. This behavior was primarily because, at lower frequencies, the reorientation of the dipoles could match the frequency variation. However, as the frequency continued to increase, its polarization mechanism (space charge polarization, and dipole orientation polarization) could not match the frequency change, resulting in an ε_r decrease with an increase in frequency. When the frequency sufficiently increased, relaxation polarization no longer had an effect on the dielectric constant, so the dielectric constant was only determined by the displacement polarization. In addition, the dielectric constant gradually decreased to the minimum value, and the dielectric loss decreased with an increase in frequency [31].

Figure 9b shows the dielectric temperature spectrum of barium titanate at different frequencies, where the sample size was 8 mm (length) × 8 mm (width) × 1 mm (height). The dielectric performance of the material was influenced by both the test temperature and test frequency, and the samples were tested at frequencies of 1 kHz, 10 kHz, 100 kHz, and 1 MHz. The dielectric performance showed an initial increase followed by a decrease as the temperature increased. At room temperature, the relative permittivity and dielectric loss at 1 kHz were 1789 and 0.014, respectively. These values were similar to those of barium titanate ceramics prepared by traditional dry pressing methods (ε_r = 1700, $tan\delta$ < 0.1) [32]. The relative permittivity and dielectric loss values obtained at room temperature were consistent with the earlier frequency spectrum measurements, indicating that the dielectric performance of the barium titanate ceramic samples was highly stable. As the

temperature increased, the relative permittivity underwent a sharp change near the Curie temperature (Tc ≈ 135 °C). At this point, the crystal structure transitioned from the ferroelectric phase to the paraelectric phase.

To characterize the polarization behavior of the samples, a ferroelectric analyzer was used to measure the hysteresis loops, where the sample size was 10 mm (length) × 10 mm (width) × 1 mm (height). The obtained remnant polarization (P_r) and coercive field (E_c) are shown in Figure 9c. The $BaTiO_3$ sample exhibited excellent ferroelectric properties. Under the influence of electric fields with values of 10 and 20 kV/cm, the remnant polarization (P_r) values were 4.5 and 7.4 μC/cm², respectively, and the coercive field (E_c) values were 2.3 and 3.5 kV/cm, respectively. P_r reflected the magnitude of polarization in the absence of an external electric field and was primarily related to the crystal grain size. Larger crystal grains resulted in larger internal domains, leading to an increase in the polarization strength [33–34]. Additionally, according to the graph, the measured hysteresis loop exhibited good saturation, indicating that the prepared barium titanate ceramic possessed significant ferroelectric properties.

After polarization, the prepared ceramic samples were tested using a d_{33} quasi-static tester, and the piezoelectric coefficient d_{33} was determined as 263 pC/N. Impedance analysis was conducted on the ceramic samples to measure the resonance frequency (f_a), anti-resonance frequency (f_r), and resistance. The ceramic sample size had dimensions of 10 mm (length) × 10 mm (width) × 1 mm (thickness), and the results yielded f_a = 593.75 kHz, f_r = 558.01 kHz, and R = 50.28 Ω. The capacitance of the sample was measured

using a precision impedance analyzer with a value of 2.78167×10^{-10} F. This information was used to calculate other electrical parameters using the following formulas:

$$K_P = \sqrt{2.51 \times \frac{f_a - f_r}{f_r}} \tag{4}$$

$$Q_m = \frac{f_r^2}{2\pi f_r RC(f_a^2 - f_r^2)} \tag{5}$$

The planar electromechanical coupling coefficient and mechanical quality factor were calculated as 0.4010 and 450, respectively, where K_P is the planar electromechanical coupling coefficient of the $BaTiO_3$ ceramics, f_a denotes the anti-resonance frequency of the samples in radial mode, f_r is the resonance frequency of the samples in radial mode, R is the equivalent resistance of ceramic specimen (Ω), and C denotes the static capacitance of the specimen (F, measured at 1 kHz).

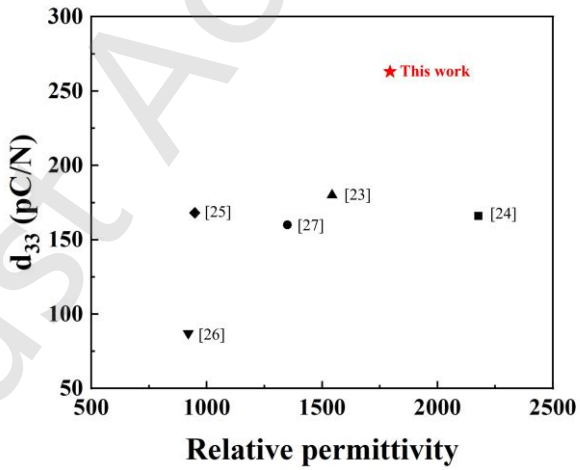

Figure 10. Comparison of the dielectric and piezoelectric properties obtained in this work with the results in the literature.

Figure 10 compares the $BaTiO_3$ ceramics in this study with other reported d_{33} and relative dielectric constants, where all samples consisted of $BaTiO_3$ ceramics prepared by

DLP 3D printing. The results showed that the $BaTiO_3$ ceramic prepared in this study had better electrical properties [35–40].

3.3. Properties of the VPP 3D printed molded porous barium titanate ceramics

In this experiment, three representative minimal surface structures were selected, namely, a Diamond structure, Gyroid structure, and Schwarz P structure. These structures were designed to exhibit the same porosity (50%). The models, green bodies, and sintered parts of these three structures are shown in Figure 11, and their specific design information is provided in Table 3.

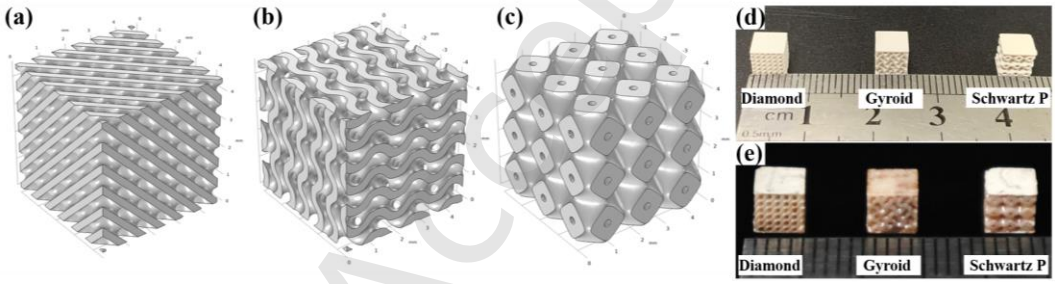

Figure 11. Model diagrams of the different minimal surface structures with 50% porosity: (a) Diamond structure; (b) Gyroid structure; (c) Schwarz P structure; sample diagrams of the different minimal surface structures with 50% porosity: (d) billet; (e) sintered part.

Table. 3 Three minimal surface parameters

Structure	Cell size (mm)	Overall size (mm)	Wall thickness (mm)	Porosity (%)
Diamond	1.5 × 1.5 × 1.5	4.5 × 4.5 ×4.5	0.17	50
Gyroid	1.5 × 1.5 × 1.5	4.5 × 4.5 × 4.5	0.21	50

Schwartz P	1.5 × 1.5 × 1.5	4.5 × 4.5 × 4.5	0.24	50

Figure 12 shows the mechanical and electrical simulation results obtained using COMSOL simulation software for the modeled structures. The material was set as barium titanate (poled), the specific physical material parameters were set according to the properties obtained in the previous test, the lower surface was set as the fixed constraint and insulation, the upper surface was given the same load (10280 N/m^2), and multiple physical fields were selected as the piezoelectric effect solid mechanics and electrostatic field. In Figure 12a–c, a color scale was used to represent the maximum stress value assumed by the entire unit, where redder portions indicated greater stress values, and whiter portions indicated smaller stress values. As shown in Figure 12 d–f, the color scale was used to represent the potential distribution of the entire unit after assuming the force and generating a piezoelectric effect, where the bluer the color, the larger the structural potential difference. According to the simulation results, we observed that the maximum stresses generated by the Diamond, Gyroid, and Schwarz P minimal surface structures with a porosity of 50% were 8.86×10^4 N/m^2, 1.18×10^5 N/m^2, and 6.24×10^4 N/m^2, respectively, with corresponding voltage values of 0.717 V, 0.792 V, and 0.642 V, respectively. The reason for these simulation results was possibly because in the structures with the same porosity, the Gyroid structure minimal surface structure could generate higher stress under the same force conditions, resulting in greater strain. For the piezoelectric materials, the piezoelectric effect generated on the surface was related to

strain. Generally, under the same stress conditions, larger strain led to better piezoelectric effects.

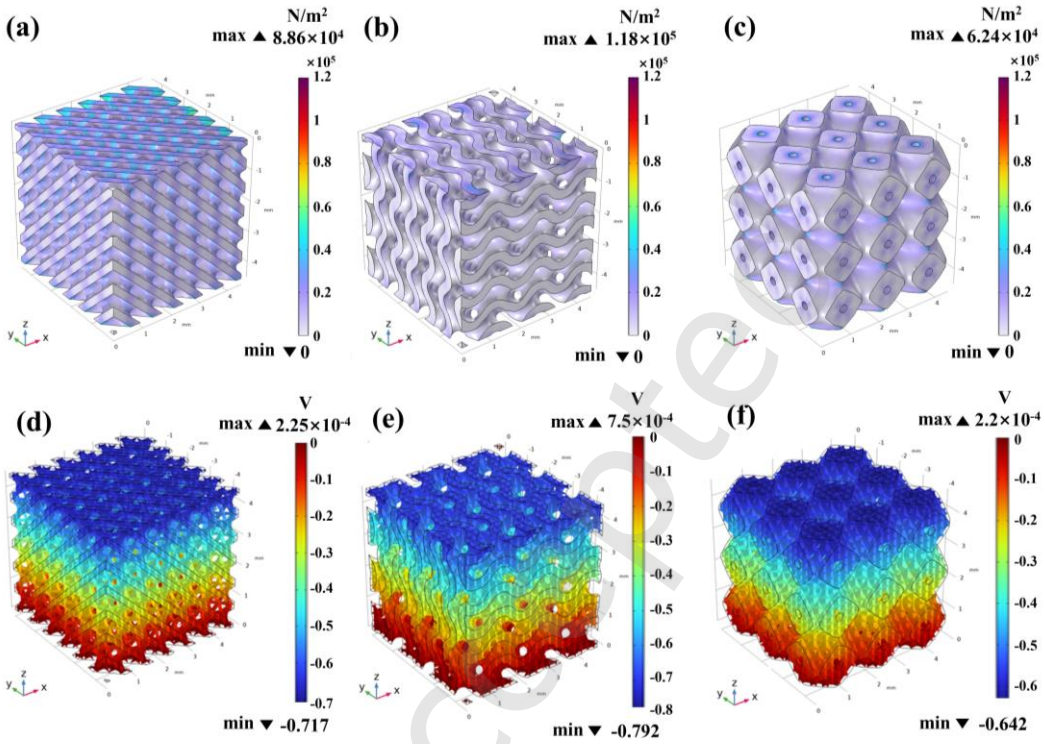

Figure 12. Plots of mechanical simulation results for (a) Diamond structure; (b) Gyroid structure; (c) Schwarz P structure; plot of the electrical simulation results for (d) Diamond structure; (e) Gyroid structure; (f) Schwarz P.

The mechanical performance of the three different minimal surface structures was tested, and the stress-strain curves are shown in Figure 13a. We observed that under the same porosity, the compressive strengths of the different structures varied. For the sample with 50% porosity, the maximum compressive strengths of the Diamond, Gyroid, and Schwarz P minimal surface structures were 58.3 ± 3.2 MPa, 37.9 ± 2.5 MPa, and 27.3 ± 1.1 MPa, respectively. The maximum compressive strengths, from highest to lowest, corresponded to the Diamond structure, Gyroid structure, and Schwarz P structure. In the

experimental results, the maximum compressive strength of the Schwarz P structure was the lowest among the three models, which was contrary to the simulation results. This was possibly due to the more obvious stress concentration points at the bonding sites between the Schwarz P structure cells and the single cells, which led to direct failure when the force exerted reached the maximum stress that the structure could bear. This was also possibly due to the large number of variables in the model, which only controlled the macro size, cell size, and porosity, but did not consider the thickness, shape, and other variables. This phenomenon will require further exploration.

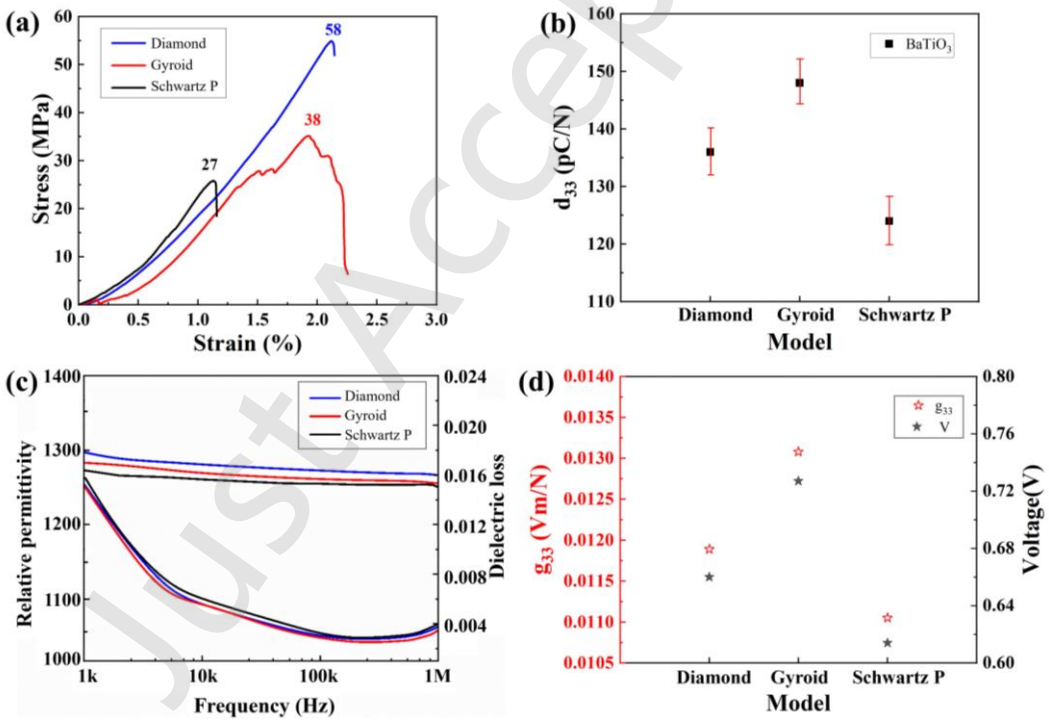

Figure 13. Characterization of the force-electric properties of $BaTiO_3$ ceramics with different minimal surface structures with 50% porosity: (a) stress-strain diagrams of the three minimal surface structures (50% porosity); (b) plot of the conformational unit versus d_{33} (50% porosity); (c) spectrograms of the different minimal surface structures

with 50% porosity; and (d) plots of g_{33}, voltage versus different minimal surfaces (porosity of 50%).

The piezoelectric performance of the three different minimal surface structures was tested and analyzed. To ensure uniform polarization within the porous structures, a 100 μm thick layer was added to both the upper and lower surfaces of the three models. A layer of silver paste was applied and polarized on one entire side of the thick layer. Subsequently, the polarized parts were analyzed for piezoelectric performance using a d_{33} quasi-static measurement instrument, where the sample size was 4.5 mm (length) × 4.5 mm (width) × 4.7 mm (thickness). The relationship between the configuration unit and the piezoelectric coefficient is shown in Figure 13b, where for the Diamond, Gyroid, and Schwarz P minimal surface structures with 50% porosity, the piezoelectric coefficients were 136 ± 5, 148 ± 5, and 124 ± 5 pC/N, respectively. The Gyroid structure exhibited the highest piezoelectric coefficient. When also considering the mechanical performance, we found that the Gyroid structure had greater strain under the same stress, which generated more electrical signals. This was consistent with the simulation results.

The dielectric performance of the three models was analyzed and tested, and the frequency spectra of the relative dielectric constant and dielectric loss at room temperature are shown in Figure 13c. We observed that at room temperature, the dielectric loss and relative dielectric constant of the structures with the same porosity did not vary significantly. The relative dielectric constants and dielectric losses for the Diamond, Gyroid, and Schwarz P minimal surface structures were tested at a frequency of 1 kHz

and measured approximately as 1292, 1278, and 1267, as well as 0.01527, 0.01513, and 0.01590, respectively. Compared to the frequency spectrum of the solid block, the relative dielectric constant significantly decreased, from around 1794 to approximately 1278. This was primarily due to the introduction of the air phase, which had a very low relative dielectric constant (1). The porous structure was essentially a composite structure of the air phase and the ceramic phase, which resulted in a lower relative dielectric constant compared to the solid block. However, the dielectric loss did not significantly decrease due to the introduction of macroscopic pores.

To compare with the simulation results, the following equations were adopted:

$$V = E \times t = -g \times X \times t = -\frac{g \times F \times t}{A} \quad (6)$$

$$g_{33} = \frac{d_{33}}{\varepsilon_r \varepsilon_0} \quad (7)$$

where V is the open circuit output voltage (V) of the ceramic, E is the electric field (V/m), t is the thickness of the ceramic (m), g_{33} is the piezoelectric voltage constant (Vm/N), F is the applied force (N), and A is the cross-sectional area (m^2) of the ceramic under stress. The V and g_{33} values of three minimal surface structures were calculated. During the testing of the piezoelectric coefficient d_{33}, the force applied by the testing of the instrument's vibrations was approximately 0.25 N. The results in Figure 13d were obtained through calculation. In the Diamond, Gyroid, and Schwarz P minimal surface structures with 50% porosity, the g_{33} values were approximately 1.189×10^{-2}, 1.308×10^{-2}, and 1.105×10^{-2} Vm/N, respectively, and the calculated voltages were approximately 0.660 V, 0.727 V, and 0.614 V, respectively. This was consistent with the

simulation results, indicating that the order of increasing electrical signals produced by the minimal surface structures with the same porosity was as follows: Gyroid structure, Diamond structure, and Schwarz P structure.

According to the analysis of the results, when comparing the three structures with the same porosity, the Diamond structure exhibited the best mechanical performance, while the Gyroid structure had the best piezoelectric performance. The differences in dielectric properties (relative permittivity and dielectric loss) among the structures were not significant. In terms of energy harvesting parameters, structures with larger piezoelectric coefficients, smaller relative permittivity, and lower dielectric loss were preferable as they could achieve higher energy harvesting efficiency. Therefore, in this experiment, the Gyroid structure was selected as the optimal 3-3 type porous structure.

Based on the selected 3-3 type Gyroid minimal surface structure, different three-dimensional model structures with varying porosities were designed. Considering the requirements for lightweight and miniaturized applications, as well as the minimum wall thickness achievable through light-curing shaping, five Gyroid minimal surface structures with porosities of 50%, 55%, 60%, 65%, and 70% were designed. The specific model parameters for these structures are provided in Table 4. The models, as shown in Figure 14, ranged in porosity from 50% to 70% and included the model, green body, and sintered part images.

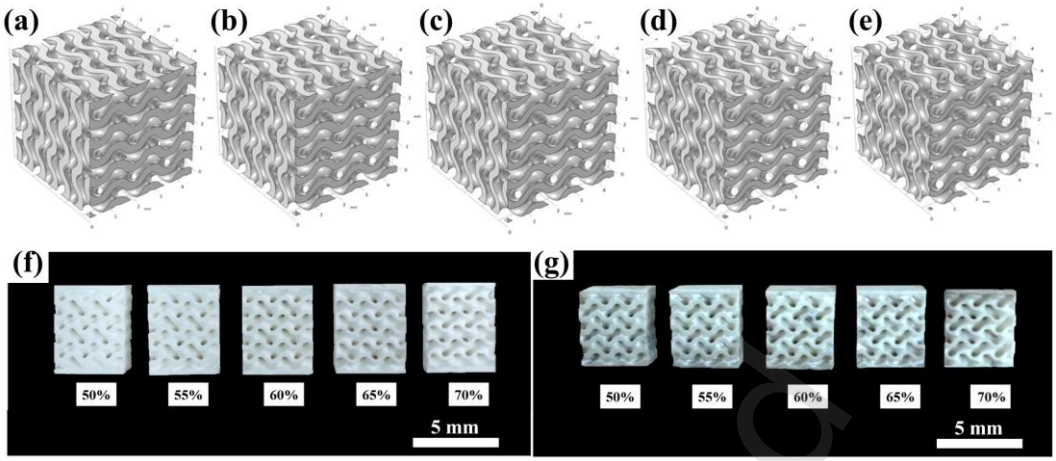

Figure 14. Model diagrams of the Gyroid minimal surface structures with different porosities: (a) 50%; (b) 55%; (c) 60%; (d) 65%; (e) 70%; sample diagrams of the Gyroid minimal surface structures at different porosities: (a) billet; (b) sintered part.

Table. 4 Three minimal surface parameters

Structure	Cell size (mm)	Overall size (mm)	Wall thickness (mm)	Porosity (%)
Gyroid	1.5 × 1.5 × 1.5	4.5 × 4.5 × 4.5	0.21	50
Gyroid	1.5 × 1.5 × 1.5	4.5 × 4.5 × 4.5	0.19	55
Gyroid	1.5 × 1.5 × 1.5	4.5 × 4.5 × 4.5	0.17	60
Gyroid	1.5 × 1.5 × 1.5	4.5 × 4.5 × 4.5	0.15	65
Gyroid	1.5 × 1.5 × 1.5	4.5 × 4.5 × 4.5	0.13	70

Finite element simulations of the five models were conducted in terms of mechanical and electrical aspects, and the simulated results for stress and surface voltage generation are presented in Figure 15a–j. After analyzing the mechanical simulation results, we determined that the maximum stress values for structures with different porosities were

as follows: 1.18×10^5 N/m^2, 1.30×10^5 N/m^2, 1.49×10^5 N/m^2, 3.73×10^5 N/m^2, and 3.86×10^5 N/m^2. Brittle fracture of ceramics often occurs at stress concentration points, and structures with lower maximum stress will have greater resistance to deformation. Thus, we observed that under the same boundary conditions and structures, the maximum stress increased with increasing porosity, indicating that higher porosity made fracture more likely to occur. According to the electrical simulation results, the absolute values of surface voltage generated for porosities of 50%, 55%, 60%, 65%, and 70% were 0.792, 0.793, 0.798, 0.802, and 0.812V, respectively, where the generated voltage increased with increasing porosity. According to Equation (3), the generated voltage was directly proportional to the piezoelectric coefficient and inversely proportional to the relative permittivity. From the simulation results, we found that the voltage increased with increasing porosity. This was because the introduction of porosity led to a reduction in both the piezoelectric coefficient and relative permittivity, however, the relative permittivity decreased faster than the piezoelectric coefficient, resulting in an increase in generated voltage with increasing porosity.

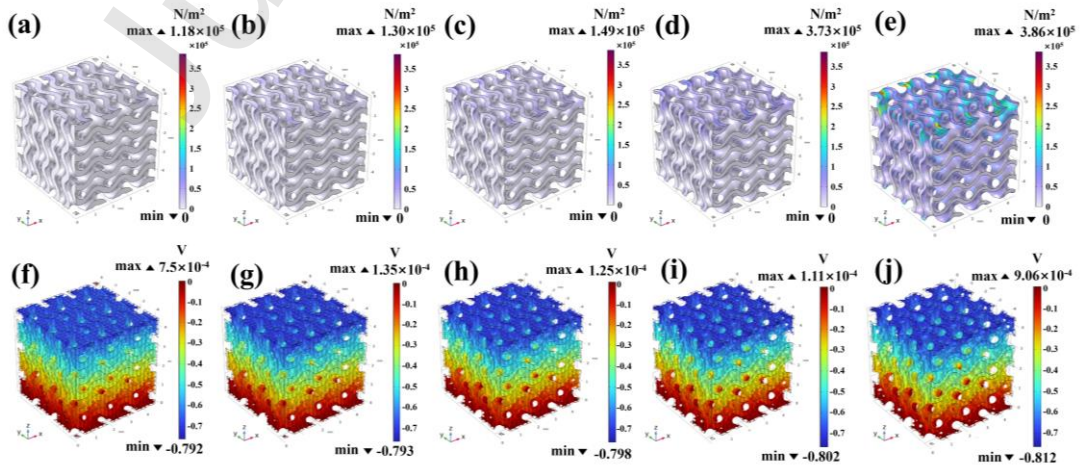

Figure 15. Plots of the mechanical simulation results of the Gyroid structures with porosities of (a) 50%; (b) 55%; (c) 60%; (d) 65%; (e) 70%; electrical simulation results of the Gyroid structures with porosities of (f) 50%; (g) 55%; (h) 60%; (i) 65%; (j) 70%.

Mechanical performance testing was conducted on Gyroid structures with different porosities and the stress-strain curves are shown in Figure 16a. We observed that as the porosity increased, the maximum strain gradually decreased, and the maximum stress that could be sustained also decreased. The maximum compressive strengths at porosities of 50%, 55%, 60%, 65%, and 70% were 37.9 ± 2.5, 29.2 ± 1.8, 27.8 ± 1.5, 22.7 ± 1.2, and 18.6 ± 0.8 MPa, respectively. The stress and strain increased linearly, showing elastic deformation in the initial stage. As the external load gradually increased, stress fluctuations occurred due to the unique lattice structures and the presence of porosity in the Gyroid structures. When all lattice structures reached their pressure limits, brittle fracture occurred.

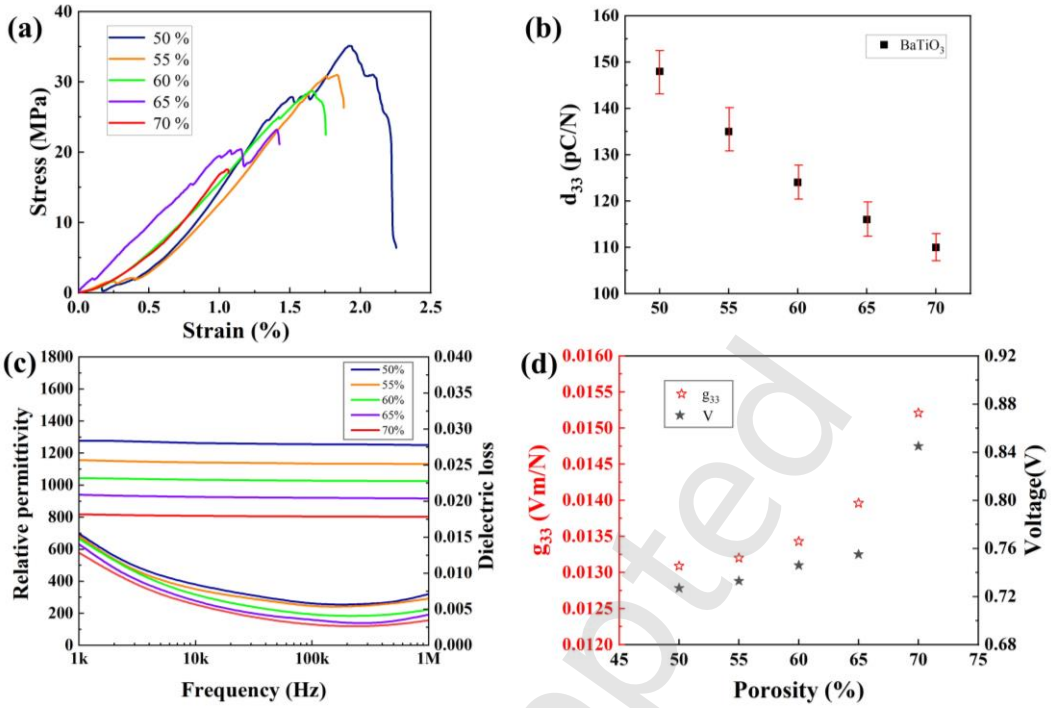

Figure. 16. Characterization of the force-electric properties of the $BaTiO_3$ ceramics with Gyroid structures at different porosities: (a) stress-strain plots with different porosities; (b) plots of porosity versus d_{33}; (c) spectrograms of the Gyroid structures with different porosities; (d) plots of g_{33}, voltage vs. different porosities.

Testing and analysis of the piezoelectric properties of the Gyroid structures with different porosities were conducted, and the relationship between the porosity and piezoelectric coefficient is shown in Figure 16b. The piezoelectric coefficients of different porosity are 148 ± 5, 135 ± 5, 124 ± 4, 116 ± 4 and 110 ± 3 pC/N, respectively. The piezoelectric coefficient of porous piezoelectric ceramics is significantly lower than that of solid blocks. With the increase of porosity, the piezoelectric coefficient gradually decreases, which is contrary to the change law of the electric potential difference in the simulation result. This is because the decrease of wall thickness caused by the increase of

porosity is not considered in the simulation, resulting in the deterioration of the actual polarization effect, and then the piezoelectric coefficient decreases.

The dielectric properties of the above five Gyroid structures with different porosities were analyzed and tested, and the spectra of relative permittivity and dielectric loss at room temperature were obtained, as shown in Figure 16c. The relative permittivity and dielectric loss of the five structures with porosity ranging from 50% to 70% were 1278, 1156, 1043, 939, and 817; 0.0159, 0.0161, 0.0166, 0.0169, and 0.0175, respectively. The relative permittivity gradually decreased with increasing porosity, while the dielectric loss barely changed.

The simulation results were compared with the experimental results for analysis of the piezoelectric values at different porosities of the Gyroid structures. The V and g_{33} values at different porosities of the Gyroid structures were calculated by Equations (3) and (4), and the relationship was plotted, as shown in Figure 16d. The g_{33} of the Gyroid structures with very small surface structures at porosities of 50%, 55%, 60%, 65%, and 70% were 1.309×10^{-2} Vm/N, 1.320×10^{-2} Vm/N, 1.343×10^{-2} Vm/N, 1.396×10^{-2} Vm/N, and 1.521×10^{-2} Vm/N, and the calculated voltages were 0.727 V, 0.733 V, 0.746 V, 0.775 V, 0.845 V, respectively. We observed that the piezoelectric voltage constants and the voltage values gradually increased with increasing porosity, which was in line with the trend of the simulation results. Therefore, under the same stress conditions, the larger the porosity of the same structure, the larger the value of the voltage generated.

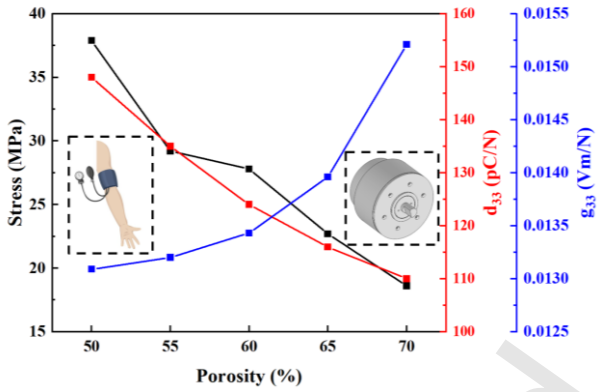

Figure 17. Analysis of the piezoelectric properties and the applications of $BaTiO_3$ ceramics with Gyroid structures at different porosities.

Based on the comprehensive analysis of the piezoelectric properties of different porosities for the Gyroid structures, as shown in Figure 17, when the porosities were 50%, 55%, and 60%, the ceramic exhibited high compressive strength, d_{33} values, and lower g_{33} values. This made it suitable for applications in environments where external pressure or strain had to be converted into charge signals, such as pressure sensors, seismic detectors, and energy harvesters for high-pressure and high-strain environments. However, when the porosities were 65% and 70%, the ceramic exhibited lower compressive strength and d_{33} values but higher g_{33} values. This configuration was well-suited for specific applications that require high precision, sensitivity, and high-frequency performance, such as piezoelectric ceramic motors, vibration controllers, and microelectromechanical systems. In summary, the choice of porosity in the Gyroid structures allowed for tailoring of the material's properties for a wide range of applications, from high-pressure and high-strain environments to high-precision and high-frequency applications.

4. Conclusions

In this work, we systematically investigated the preparation process of high-performance $BaTiO_3$ ceramics using VPP technology. The study included the design of the ceramic slurry composition, the forming process, post-processing of the green bodies, and their applications. The main research findings were summarized as follows.

1) Successfully utilizing VPP 3D printing technology to fabricate $BaTiO_3$ piezoelectric ceramic green bodies.

2) This study explored optimal ceramic slurry formulation by analyzing the influence of various sintering regimes on the ceramic forming quality and we subsequently investigated the impact of density on ceramic samples. The optimal sintering regime was established, initially ramping to 1400 °C, followed by relatively rapid cooling to 1200 °C, holding for 15 h, and then gradually cooling in the furnace. The resulting maximum density achieved was 96.3%.

3) Under the optimal sintering regime, this study analyzed various performance parameters of the ceramics. The ceramic exhibited a compressive strength of 250 ± 25 MPa and a maximum three-point flexural strength of 45 ± 8 MPa. When tested at room temperature with a frequency of 1 kHz, the relative dielectric constant and dielectric loss were determined as 1794 and 0.014, respectively. The Curie temperature was approximately 135 °C, demonstrating good ferroelectric properties. The piezoelectric coefficient (d_{33}) was measured at 263 pC/N, and the planar electromechanical coupling coefficient and mechanical quality factor were 0.4010 and 450, respectively.

4) Three different minimal surface structures were designed by employing modeling software and subjected to mechanical and electrical performance simulations. Additionally, porous Gyroid structures minimal surface structures with porosities ranging from 50% to 70% were designed and subjected to simulations and experimental verification. The piezoelectric coefficient gradually decreased, the relative dielectric constant decreased, compressive strength decreased, and the piezoelectric voltage constant gradually increased, resulting in an increase in piezoelectric output.

Declaration of competing interest

The authors have no competing interests to declare that are relevant to the content of this article.

Data availability

Data will be made available on request.

Acknowledgements

This research was sponsored by the Beijing Municipal Science and Technology Project (KM202010005003), the Sponsored by Beijing Nova Program (20220484008) and General Program of Science and Technology Development Project of Beijing Municipal Education Commission.

References

[1] Acosta M, Novak N, Rojas V, Patel S, Vaish R, Koruza J, Rossetti GA, et al. $BaTiO_3$-based piezoelectrics: Fundamentals, current status, and perspectives. Appl. Phys. Rev. 2017, 4: 041305.

[2] Jing Q, Li XJ. Preparation of porous barium titanate ceramics and enhancement of piezoelectric sensitivity. Acta Phys. Sin. 2019, 68(5): 057701.

[3] Jain A, Wang YG, Shi LN, Recent developments in $BaTiO_3$ based lead-free materials for energy storage applications. J. Alloys Compd 2022, 928: 167066.

[4] Beak K, Choi M, Kim DH, et al. Silane-treated $BaTiO_3$ ceramic powders for multilayer ceramic capacitor with enhanced dielectric properties. Chemosphere 2022, 286: 131734.

[5] Huan Y, Wang XH, Fang J, Li LT. Grain Size Effects on Piezoelectric Properties and Domain Structure of $BaTiO_3$ Ceramics Prepared by Two-Step Sintering[J]. J. Am. Ceram. Soc. 2013, 96(11): 3369-3371.

[6] Kalyani AK, Brajesh K, Senyshyn A, et al. Orthorhombic-tetragonal phase coexistence and enhanced piezo-response at room temperature in Zr, Sn, and Hf modified $BaTiO_3$[J]. Appl. Phys. Lett. 2014, 104(25): 252906.

[7] Yang Y, Zhou YB, Ren J, et al. Coexistence of three ferroelectric phases and enhanced piezoelectric properties in $BaTiO_3$ –$CaHfO_3$ lead-free ceramics. J. Eur. Ceram. Soc. 2018, 38(2): 557-566.

[8] Zhang LH, Liao YW, Liu YF, et al. Preparation and properties of $Bi_{0.5}$ $(Na_{0.7}K_{0.2}Li_{0.1})_{0.5}TiO_3$ porous piezoelectric ceramics. Journal of Xihua Normal University (Natural Science Edition) 2012, 33(04): 382-385.

[9] Li ZK. Preparation, structure and properties of 3-3 piezoelectric composites. Shaanxi: Xi'an University of Science and Technology 2010.

[10] Simunec DP, Breedon M, Muhammad FUR, et al. Electrical capability of 3D printed unpoled polyvinylidene fluoride (PVDF)/thermoplastic polyurethane (TPU) sensors combined with carbon black and barium titanate [J]. Addit Manuf 2023, 73: 103679.

[11] Chen F, Yang C, An Z, et al. Direct-ink-writing of multistage-pore structured energy collector with ultrahigh ceramic content and toughness [J]. Materials & Design 2022, 217: 110652.

[12] Sotov A, Kantyukov A, Popovich A, et al. LCD-SLA 3D printing of $BaTiO_3$ piezoelectric ceramics [J]. Ceramics International 2021, 47(21): 30358–30366

[13] Zhao YT, Li PR, Dong P, et al. Investigation on 3D printing ZrO_2 implant abutment and its fatigue performance simulation. Ceram. Int. 2021, 47: 1053-1062.

[14] Lu J, Peng D, Zhao Y, et al . 3D printing of TPMS structural ZnO ceramics with good mechanical properties. Ceram. Int. 2021, 47: 12897-12905.

[15] Xiong S, Liu J, Cao J, et al. 3D printing of crack-free dense polymer-derived ceramic monoliths and lattice skeletons with improved thickness and mechanical performance [J]. Addit Manuf 2022, 57: 102964.

[16] Wei X, Jin ML, Yang H, et al. Advances in 3D printing of magnetic materials: Fabrication, properties, and their applications [J]. J. Adv. Ceram. 2022, 11(5): 665–701.

[17] He R, Liu W, Wu Z, et al. Fabrication of complex-shaped zirconia ceramic parts via a DLP- stereolithography-based 3D printing method[J]. Ceram. Int. 2018, 44: 3412-3416.

[18] Cortés A, Sánchez-Romate X, Jiménez-Suárez A. Complex geometry strain sensors based on 3D printed nanocomposites: spring, three-column device and footstep-sensing platform[J]. Nanomaterials 2021, 5: 1106.

[19] Guerra AJ, Lara-Padilla H, Becker ML. Photopolymerizable resins for 3D-printing solid-cured tissue engineered implants[J]. Curr Drug Targets 2019, 20(8): 823-838.

[20] Sun J, Zhang J, Zhang X, et al. High strength mullite-bond SiC porous ceramics fabricated by digital light processing [J]. J. Adv. Ceram. 2024, 13(1): 53–62.

[21] Zhang X, Zhang K, Zhang B, et al. Mechanical properties of additively-manufactured cellular ceramic structures: A comprehensive study [J]. J. Adv. Ceram. 2022, 11(12): 1918–1931.

[22] Chen AN, Li M, Wu JM, et al. Enhancement mechanism of mechanical performance of highly porous mullite ceramics with bimodal pore structures prepared by selective laser sintering. J. Alloys Compd, 2019, 776C:486-494.

[23] Chen R, Duan W, Wang G. Preparation of broadband transparent Si_3N_4-SiO_2 ceramics by digital light processing (DLP) 3D printing technology[J]. J. Eur. Ceram. Soc. 2021, 41: 5495-5504.

[24] Chen Z, Sun X, Shang Y. Dense ceramics with complex shape fabricated by 3D printing: a review[J]. J. Adv. Ceram. 2021, 10: 195-218.

[25] Yao Y, Qin W, Xing B, et al. High performance hydroxyapatite ceramics and a triply periodic minimum surface structure fabricated by digital light processing 3D printing [J]. J. Adv. Ceram. 2021, 10(1): 39–48.

[26] Liu K, Sun Y, Sun H, et al. Effect of particle grading on the properties of photosensitive slurry and BaTiO3 piezoelectric ceramic via digital light processing 3D printing [J]. Journal of the European Ceramic Society 2023, 43(8): 3266–3274.

[27] Jiang ZJ, Cheng LY, Zeng Y, et al. 3D printing of porous scaffolds $BaTiO_3$ piezoelectric ceramics and regulation of their mechanical and electrical properties. Ceram. Int. 2022, 48(5): 6477-6487.

[28] Huang YA, Lu B, Zou YX, et al. Effect of grain size on dielectric, piezoelectric and ferroelectric properties of fine-crystalline barium titanate ceramics. Inorg. Mater. 2018, 33(07): 767-772.

[29] Priya S. Criterion for material selection in design of bulk piezoelectric energy harvesters. IEEE transactions on ultrasonics, ferroelectrics, and frequency control 2010, 57(12): 2610-2612.

[30] Wang XH, Deng XY, Bai HL, et al. Two-step sintering of ceramics with constant grain-size, II: $BaTiO_3$ and Ni-Cu-Zn ferrite. J. Am. Ceram. 2006, 89(2): 438–443.

[31] Sato S, Nakano Y, Sato A, et al. Mechanism of improvement of resistance degradation in Y-doped $BaTiO_3$ based MLCCs with Ni electrodes under highly accelerated life testing. J. Eur. Ceram. Soc. 1999, 19: 1061-1065.

[32] Vijatovic MM, Bobic JD, Stojanovic BD. History and challenges of barium titanate: part II. Sci. Sinter. 2008, 40 (3): 235–244.

[33] Sandi DK, Supriyanto A, Anif, et al. The effects of sintering temperature on dielectric constant of Barium Titanate ($BaTiO_3$). IOP Conference Series: Materials Science and Engineering 2016, 107(1).

[34] Cai W. Preparation, microstructure and dielectric properties of barium titanate-based ceramics. Chongqing University, 2011.

[35] Liu C-L, Du Q, Zhang C, et al. Fabrication and properties of $BaTiO_3$ ceramics via digital light processing for piezoelectric energy harvesters [J]. Additive Manufacturing 2022, 56: 102940.

[36] Cheng J, Chen Y, Wu J-W, et al. 3D Printing of $BaTiO_3$ Piezoelectric Ceramics for a Focused Ultrasonic Array [J]. Sensors 2019, 19(19): 4078.

[37] Liu K, Zhou C, Hu J, et al. Fabrication of barium titanate ceramics via digital light processing 3D printing by using high refractive index monomer [J]. Journal of the European Ceramic Society 2021, 41(12): 5909–5917.

[38] Song X, Chen Z, Lei L, et al. Piezoelectric component fabrication using projection-based stereolithography of barium titanate ceramic suspensions [J]. Rapid Prototyping Journal 2017, 23(1): 44–53.

[39] Chen X, Sun J, Guo B, et al. Effect of the particle size on the performance of $BaTiO_3$ piezoelectric ceramics produced by additive manufacturing [J]. Ceramics International 2022, 48(1): 1285–1292.

[40] Chen Z, Song X, Lei L, et al. 3D printing of piezoelectric element for energy focusing and ultrasonic sensing [J]. Nano Energy 2016, 27: 78–86.